Synthesis and characterization of high surface area TiO2/SiO2 mesostructured nanocomposite

Magali Bonne, Stéphane Pronier, Fabien Can, Xavier Courtois, Sabine Valange, Jean-Michel Tatibouët, Sébastien Royer, Patrice Marecot, Daniel Duprez

▶ **To cite this version:**

Magali Bonne, Stéphane Pronier, Fabien Can, Xavier Courtois, Sabine Valange, et al.. Synthesis and characterization of high surface area TiO2/SiO2 mesostructured nanocomposite. Solid State Sciences, 2010, 12 (6), pp.1002-1012. 10.1016/j.solidstatesciences.2009.10.009 . hal-04164450

HAL Id: hal-04164450
https://hal.science/hal-04164450

Submitted on 13 Nov 2023

HAL is a multi-disciplinary open access archive for the deposit and dissemination of scientific research documents, whether they are published or not. The documents may come from teaching and research institutions in France or abroad, or from public or private research centers.

L'archive ouverte pluridisciplinaire **HAL**, est destinée au dépôt et à la diffusion de documents scientifiques de niveau recherche, publiés ou non, émanant des établissements d'enseignement et de recherche français ou étrangers, des laboratoires publics ou privés.

Synthesis and characterization of high surface area TiO_2/SiO_2 mesostructured nanocomposite

BONNE Magali, PRONIER Stéphane, CAN Fabien, COURTOIS Xavier, VALANGE Sabine, TATIBOUET Jean-Michel, ROYER Sébastien,* MARECOT Patrice, DUPREZ Daniel

LACCO, UMR 6503 CNRS, 40 Avenue du Recteur Pineau, 86022 Poitiers Cedex France.

*, Author to whom correspondences should be addressed

Tel: +33 549453479, fax: +33 549453741, Email: sebastien.royer@univ-poitiers.fr

Abstract

Recently titania synthesis was reported using various structuration procedures, leading to the production of solid presenting high surface area but exhibiting moderate thermal stability. The study presents the synthesis of TiO_2/SiO_2 nanocomposites, a solid that can advantageously replace bulk titania samples as catalyst support. The silica host support used for the synthesis of the nanocomposite is a SBA-15 type silica, having a well-defined 2D hexagonal pore structure and a large pore size. The control of the impregnation media is important to obtain dispersed titania crystals into the porosity, the best results have been obtained using an impregnation in an excess of solvent. After calcination at low temperature (400 °C), nanocomposites having titania nanodomains (~2-3 nm) located inside the pores and no external aggregates visible are obtained. This nanocomposite exhibits high specific surface area (close to that of the silica host support, even with a titania loading of 55 wt.%) and a narrow pore size distribution. Surprisingly, the increase in calcination temperature up to 800 °C does not allow to detect the anatase to rutile transition. Even at 800 °C, the hexagonal mesoporous structure of the silica support is maintained, and the anatase crystal domain size is evaluated at ~ 10 nm, a size close to that of the silica host support porosity (8.4 nm). Comparison of their physical properties with the results presented in literature for bulk samples evidenced that these TiO_2/SiO_2 solids are promising in term of thermal stability.

Keywords: titania, nanocomposite synthesis, physical properties, structural properties, thermal stability

1. Introduction

Due to their specific physical and chemical properties, titania-based materials are of great interest for a wide variety of applications. The chemical properties of the titanium dioxide, as well as its morphology, are intimately related to the crystallographic structure of the solid (*e.g.* rutile, anatase, brookite) [1, 2]. For instance, crystal domain of nanometric size can be obtained for the anatase polymorph while crystal transition from anatase to rutile results in a large increase in crystal domain size [3], and consequently into an important decrease in accessible specific surface area (SSA). Thus, the physical properties of the rutile form of titania become hardly compatible with a use as catalyst support [4]. The use of the anatase form of titania is then most often reported in academic studies as catalyst support [5-7] although that the use of titania, either anatase or rutile form, remains limited for high temperature reactions.

The study of titania synthesis, with the aim of obtaining a high surface area with an open porosity, is full of interest for the catalysis community. Then, many academic studies dealt with the synthesis of TiO_2 using simple precipitation routes from inorganic salts [8, 9]. Unfortunately, the physical properties of so-obtained solids remain of limited interest, and specific surface areas rarely exceed 150 $m^2.g^{-1}$ when samples are calcined for a sufficient long time to be thermally stabilized. Some more sophisticated routes based on sol-gel procedures [10-12] allow to improve in some extent the physical properties of the materials. Unfortunately, such processes do not allow to produce thermally stable samples since anatase to rutile transition occurs at similar calcination temperatures than those reported over precipitated solids, *i.e.* in the 450-550 °C temperature range [1]. With the recent developments made on the mesostructuration procedures of oxides, novel syntheses of titania presenting high surface areas and open porosities were developed. Based on the experience obtained with silica, different templating approaches, involving neutral / non-ionic or cationic templates, were proposed. Generally, the procedures involve a precipitation or a sol-gel condensation in the presence of the structuring agent. For sol-gel procedures, stabilizing agents like ethylene glycol [10] can also be used to slow down the condensation rate. Unfortunately, reactivity of the titanium towards hydrolysis and condensation reactions remains a hindrance to obtain "*well-structured*" titania solids,

and most of the studies reported a poor structuration of the solids. In spite of these constraints, amorphous or anatase crystallized samples exhibiting high surface areas are reported in the academic literature. The solids obtained by Antonelli [13] and Yoshitake et al. [14, 15] are excellent examples of these high surface area samples: TiO_2 can exhibit surface areas up to 1256 $m^2.g^{-1}$ after heat treatment at 180 °C using amine templates, while the surface areas obtained using block copolymers as templates remain lower [16-25]. Even if data concerning the thermal stability of so-obtained samples are still rare, Smarsly et al. [19] reported the synthesis of thermally stable anatase crystallized films exhibiting cubic structure. In this case, the structure is maintained up to 700 °C and the gain in thermal stability is attributed to the stability of the copolymer used towards decomposition. Some encouraging results were also obtained using cationic surfactants such as the cetyltrimethylammonium bromide (CTABr) [26-28]. However, the thermal stability of titania remains generally insufficient for a use as catalyst support in high temperature reaction whatever the synthesis route used.

Some approaches were also proposed to obtain titania-based nanocomposites. Recently, Lee et al. [29, 30] prepared a silica sol using citric acid as templating agent, in order to obtain stable supported titania nanocrystals. Titania nanocrystals are obtained during a second step by reaction of a titanium alkoxide with the fresh silica sol [30]. Elimination of the citric acid by calcination resulted in the formation of a porous high surface area titania-silica composite. The authors concluded to the formation of an anatase thin film (thickness of about 1.5 nm) on the surface of the independent silica spheres. Post grafting methods using titanium alkoxides [31] were also described. Indeed, titanium isopropoxide in toluene [32] or in hexane [33] was used to impregnate high surface area silica supports. In both cases, TiO_2 content in the final nanocomposites does not exceed 11%. The often encountered problem with post-grafting methods is the formation of external aggregates. The use of *one-pot* procedures can avoid this problem [34, 35]. Dong et al. [36] used the Evaporation Induced Self Assembly (EISA) method to achieve high TiO_2 loadings (up to 90%). The materials obtained exhibit SSA up to 290 $m^2.g^{-1}$ with large pore diameters (up to 6.8 nm). Recently, Bérubé et al. [37] reported the synthesis of Ti-doped SBA-15 materials using such *one-pot* synthesis. The material maintains high SSA and pore volume, but only a small fraction of the titania

precursor incorporates the silica matrix. Incorporation of high titania content (50 wt.%) in mesostructured silica was recently reported by Fattakhova-Rohlfing et al. [38], using pre-formed anatase nanocrystals. While the mesostructure is maintained, the surface area of the nanocomposites calcined at 300°C does not exceed 280 $m^2.g^{-1}$, with a porosity often blocked or bimodal. In this work, a SBA-15 type pure silica is used as support and composites of high TiO_2/SiO_2 ratio (55 wt.% TiO_2 on the composite) were prepared. The nanocomposites obtained are characterized using conventional characterization techniques (XRD, Raman spectroscopy, N_2-sorption experiment, TEM-EDXS), and thermal stability studied up to 800 °C.

2. Experimental section

In order to obtain homogeneous composites, *i.e.* presenting a regular dispersion of titania nanoparticles on the silica surface, an impregnation procedure using an alkoxide precursor is chosen. Indeed, a sol gel procedure is preferred to more sophisticated methods such as flash decomposition, which were used to incorporate perovskite nanocrystals inside a silica mesoporosity [39]. To allow an easy characterization of the nanocomposites, and to evidence the efficiency of the impregnation procedure, the choice of the host support is crucial. The regular pore structure of the hexagonal mesostructured materials make these solids ideal supports for impregnation. Due to the easiness of the synthesis, the SBA-15 type silica is chosen as host support. For the synthesis, all chemicals are used as received. Poly(ethylene oxide)-*b*-poly(propylene oxide)-*b*-poly(ethylene oxide) $EO_{20}PO_{70}EO_{20}$ (Pluronic P123), titanium (IV) isopropoxide ($(TiO^iPr)_4$) 97% and hydrochloric acid (HCl 32%) were purchased from Aldrich. Tetraethyl orthosilicate (TEOS) ≥99% was purchased from Fluka. Anhydrous ethanol was purchased from Merck.

The nomenclature used for the composites is defined as follow:

55Ti-SBA-y-cXXX

With: 55: TiO_2 content (in wt.%)

y: impregnation method (1, 2 or 3)

XXX: calcination temperature (°C)

2.1. Synthesis of the host support (SBA, Table 1).

The SBA-15 support is prepared according to the procedure proposed by Roggenbuck et al. [40]. A mass of 12.0 g of triblock copolymer P123 is dissolved in 360 g of water and 43 g of HCl 32 wt.%. The solution is heated at 35 °C. After the complete dissolution of the copolymer, 24 g of TEOS is slowly added under vigorous stirring given a gel composition of 1 TEOS : 0.018 P123 : 3.3 HCl : 187 H_2O (molar ratio). The transparent solution is stirred at 35 °C during 24 h. The milky solution obtained is thus transferred in a Teflon-line autoclave, and heated at 140 °C during 24 h. The autoclave is cooled down to room temperature, and the white solid filtered, washed with distilled water, and dried at 80 °C overnight. Before use and characterization, the solid is calcined under air at 550 °C during 3 h (temperature increase ramp = 1 °C.min^{-1}).

2.2. Composite synthesis.

Three different impregnation procedures were studied. In all cases, the SBA-15 freshly calcined is used as silica host support and titanium isopropoxide ($Ti(O^iPr)_4$) as titanium source. After impregnation, all the materials were calcined in a muffle furnace during 3 h at 400 °C (temperature increase rate = 1 °C.min^{-1}).

2.2.1. Impregnation method 1 (wet impregnation).

A volume of $Ti(O^iPr)_4$ corresponding to the water pore volume is slowly added to the silica host support. At the end of the precursor addition, a sticky paste is obtained. The paste is aged under ambient conditions until a dry powder is obtained. Thereafter, the solid is transferred to an oven at 80 °C for one night.

2.2.2. Impregnation method 2 (wet impregnation).

The method 2 is based on the impregnation method 1, except that titanium precursor is first diluted in absolute ethanol. A known volume of $Ti(O^iPr)_4$ is then dissolved in the same volume of absolute ethanol (volume ratio $V_{Ti(OiPr)4}/V_{EtOH}$ = 1). After homogenization, the solution is slowly added to the host support. The solvent is evaporated under ambient conditions, and the solid dried at 80 °C for one night. Impregnation procedure is repeated twice to achieve the desired TiO_2 loading (55 wt.%).

2.2.3. Impregnation method 3 (impregnation in excess of solvent).

This method consists in the slow impregnation of a dilute solution of $Ti(O^iPr)_4$ in dry ethanol (volume ratio $V_{Ti(OiPr)4}/V_{EtOH}$ = 0.2). A solution of $Ti(O^iPr)_4$ / ethanol (the volume of titanium isopropoxide is adjusted to obtain the desired TiO_2 loading) is first prepared. A known volume of solution (depending on the desired titania loading) is slowly added to the silica support. The solvent is evaporated under stirring at room temperature, and the solid aged one day under ambient conditions. Thereafter, the aged solid is transferred into an oven at 80 °C for one night. The impregnation procedure is repeated a second time to obtain the desired TiO_2 content.

To summarize, one sample is obtained by wet impregnation of $Ti(O^iPr)_4$ (55Ti-SBA-1), another one by wet impregnation of $Ti(O^iPr)_4$ in ethanol (55Ti-SBA-2), and the last one by impregnation of $Ti(O^iPr)_4$ in an excess of solvent (55Ti-SBA-3).

2.3. Characterization

Powder wide angle and small angle XRD patterns are obtained on a Bruker AXS D5005 X-ray diffractometer, using a CuKα radiation (λ = 1.54184 Å) as X-ray source. For small-angle analysis, signal is recorded for 2θ comprised between 0.75° and 3° with a step of 0.01° (step time of 10 s). From wide-angle analysis, signal is recorded for 2θ comprised between 10° and 80° with a step of 0.05° (step time of 2 s). Phase identification is made by comparison with JCPDS database. If diffraction peaks attributed to the anatase structure are detected in the wide angle region, crystal domain size is estimated using the Scherrer equation after Warren's correction for instrumental broadening: $D = \frac{K.\lambda}{\beta.\cos\theta}$. K is a constant assumed equal to 0.86 and λ is the wavelength of the X-ray source. β is the effective linewidth of the X-ray reflexion, calculated by the formula $\beta^2 = B^2 - b^2$ where B is the FWHM of the reflection and b is the instrumental broadening determined by the FWHM of X-ray reflection of quartz having particles larger than 150 nm.

Specific surface area, pore size distribution and pore volume are obtained from N_2 sorption experiments. A known mass of about 0.150 g of sample is first heat treated under vacuum 6 h at 250 °C. Isotherms are obtained at -196 °C on a Micromeritics TRISTAR instrument. The specific surface area, S_{BET}, was

calculated from the linear part of the BET plot. The mesopore size distribution was determined from the desorption branch of the isotherms using the Barrett–Joyner–Halenda (BJH) model. Mesopore volume is determined on the isotherms at P/P_0 = 0.97.

The pore structure, as well as TiO_2 particle distribution inside the silica grain, is evaluated by TEM coupled with Energy Dispersive X-ray spectroscopy (EDXS). Micrographs are obtained on a JEOL 2100 instrument (operated at 200 kV with a LaB_6 source and equipped with a Gatan Ultra scan camera). Information concerning titania dispersion inside silica (TiO_2/SiO_2 ratio at different zones of the sample) are obtained by EDX spectroscopy on the same instrument. Analysis was repeated on several silica grains to accede to a mean value of TiO_2/SiO_2 ratio. This allows us to verify if impregnation resulted in a satisfying dispersion of titania into the different silica grains or if titania segregates at the outer layers of silica.

All data from Raman analysis are collected on a LabRAM HR 800 spectrometer from Horiba Jobin Yvon with a BXFM microscope. Raman scattering was excited with a 514.5 nm excitation wavelength. The spectral area used is from 50 to 800 cm^{-1}.

IR spectra are recorded on a Nicolet Nexus spectrometer equipped with a DTGS (Deuterium TriGlyceride Sulfur) detector and a KBr beamsplitter using a resolution of 4 cm^{-1} and 64 scans. Samples were pressed as self-supported wafers. Discs of 10 $mg.cm^{-2}$ were prepared and treated directly in the cell. The samples were firstly activated under oxygen flow (100 $mL.min^{-1}$) up to 400 °C (temperature increase rate = 5 $°C.min^{-1}$) during 1 hour before being evacuated under dynamic vacuum for 15 min and finally cooled down at ambient temperature. To analyze the structure of the nanocomposites, spectra were recorded on wafers containing sample powder diluted in KBr (1:100 wt.%).

3. Results

3.1. Physical and textural properties of the silica host support.

The SBA-15 sample presents a type IV isotherm (according to the IUPAC classification [41]), clearly identified by parallel adsorption and desorption branches. A long adsorption plateau is also observed at high P/P_0 (Fig. 1).

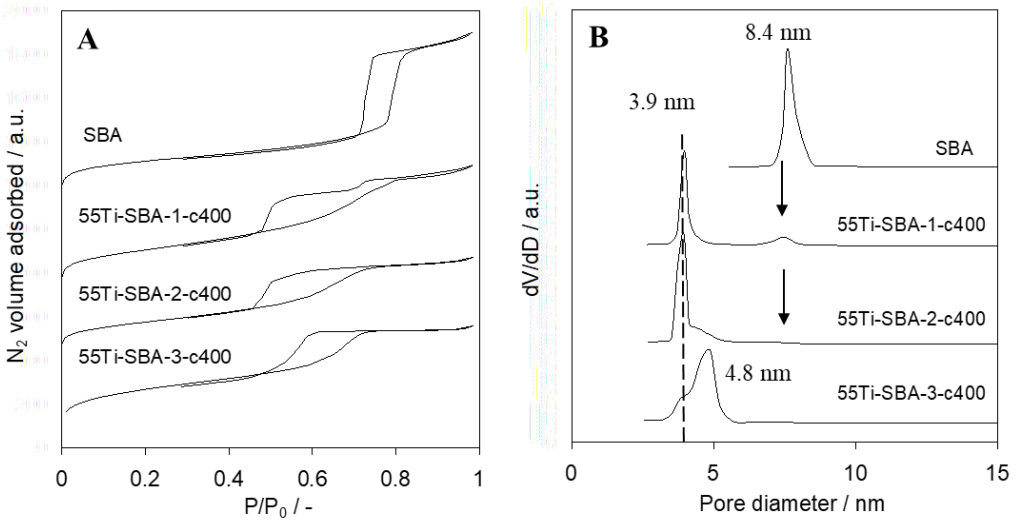

Fig. 1. N_2 adsorption – desorption isotherms and corresponding BJH pore size distribution obtained for the SBA-15 host support and the nanocomposites calcined at 400 °C.

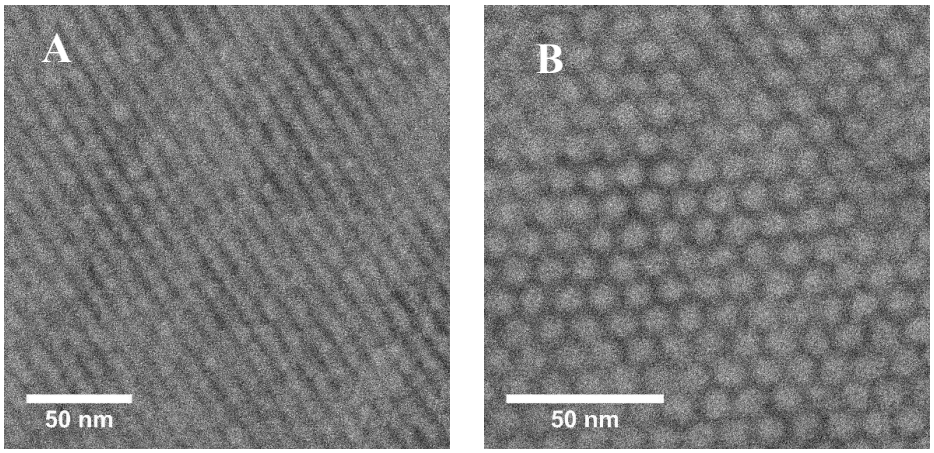

Fig. 2. TEM images obtained for the SBA-15 silica host support.

Table 1. Physical properties of the samples.

Sample name	S_{BET}[a] ($m^2.g^{-1}$)	V_{meso}[a] ($cm^3.g^{-1}$)	V_{micro}[a] ($cm^3.g^{-1}$)	D_p[a] (nm)	d_{100}[b] (nm)	Wall thickness[c] (nm)	Crystal phase / d_{XRD}[d] (nm)
SBA	470	1.13	0.061	8.4	9.6	5.2	-
55Ti-SBA-1-c400	360	0.45	0.015	3.9 – 7.5	9.6	9.7 – 6.1	Anatase / 36.5
55Ti-SBA-2-c400	307	0.35	0.015	3.9	9.6	9.7	Anatase / 17.1
55Ti-SBA-3-c400	482	0.47	0.072	4.8	9.6	8.8	n.d.

[a], S_{BET} is the specific surface area obtained using the BET model, V_{meso} is the mesopore volume measured at P/P0 = 0.97, V_{micro} is the micropore volumeextrapolated from the t-plots, D_p is the mean pore diameter obtained using the BJH model on the desorption branch; [b], d_{100} is the lattice spacing obtained using low angle XRD; [c], wall thickness is calculated for a hexagonal system : $a_0 - D_p$; with a_0 lattice parameter $a_0 = (2\ d_{100})/\ \sqrt{3}$; [d], crystal phase identified by XRD (n.d.: no phase detected) and d_{XRD} is the crystal domain size evaluated from the X-ray line broadening using the Scherrer equation.

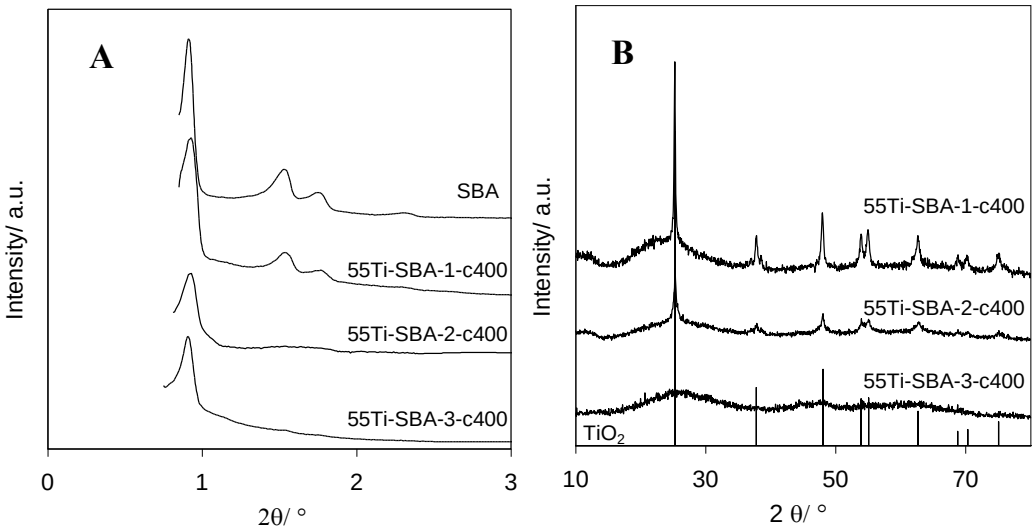

Fig. 3. X-ray diffraction patterns obtained for the nanocomposites calcined at 400 °C.

The specific surface area (SSA), evaluated using the BET equation, is 470 $m^2.g^{-1}$, and the mean pore diameter, determined on the desorption branch using the BJH equation, is 8.4 nm. The N_2 pore volume is measured at 1.13 $cm^3.g^{-1}$ (Table 1). As often reported in the literature, t-plot evidences the presence of some microporosity originating from the hydrophilic nature of poly(ethylene oxide) (PEO) blocks of the template [42, 43], even if the sample is autoclaved at high temperature (140 °C). All these physical properties, *i.e.* the high pore volume and large pore size, as well as the high specific surface area, make this support an excellent candidate for titania impregnation up to high loadings. X-ray diffraction pattern obtained in the low 2θ region clearly evidences three diffraction peaks, characteristic of the *(100)*, *(110)* and *(200)* diffraction planes of the hexagonal pore structure (Fig. 3A). This suggests a sample having a well-defined structure. The corresponding lattice spacing estimated on the *(100)* diffraction peak is 9.6 nm, and the calculated wall thickness is 5.2 nm (Table 1). TEM confirms the formation of a well-defined hexagonal structure (Fig. 2). Indeed, arrays (Fig. 2A) and the hexagonal symmetry of the pores (Fig. 2B) are clearly observed whatever the zone of the sample analyzed. The typical morphology of the hexagonal silica samples, easily observed by TEM is also a great advantage since the maintain of the structure and the localization of titania clusters can easily be deduced from TEM analysis and can complete information deduced from N_2 sorption experiments and X-ray diffraction analyses.

3.2. Physical properties of the composites

Impregnation procedure can results in some segregation of the impregnation phase outside the support, especially at high loading. Moreover, the use of a hexagonal silica support, presenting a 2D pore structure, can also be a constraint. Indeed, a satisfying dispersion of the impregnated phase inside the silica pores can be obtained only if impregnation media infiltrates the whole pore volume before precipitation, or deposition, of the phase precursor (in our case $Ti(O^iPr)_4$). We present here the results obtained changing the impregnation procedure (from wet impregnation to impregnation in excess of solvent), to evidence the crucial role of the impregnation steps on the *"quality"* of the composites obtained after thermal treatment.

A comparison between the three ways of impregnation is given with only 55 wt.% of titania in silica, a high titania loading. As observed in Table 1, the three samples present large differences in term of physical properties. Specific surface area is found to vary between 307 $m^2.g^{-1}$ (using wet impregnation of $Ti(O^iPr)_4$, 55Ti-SBA-1-c400) and 482 $m^2.g^{-1}$ (using impregnation of a dilute $Ti(O^iPr)_4$ solution, 55Ti-SBA-3-c400). For impregnation route 3 (55Ti-SBA-3-c400), the specific surface area of the solid remains in the same range than that obtained for the silica support. Conversely, the two other impregnation routes (1 and 2) lead to significant decrease in specific surface area. A decrease in mesopore volume (V_{meso}, Table 1), from 1.13 $cm^3.g^{-1}$ (SBA) to 0.35-0.47 $cm^3.g^{-1}$ (composites), is observed after impregnation (Table 1 and Figure 1). The micropore volume (V_{micro}, Table 1), evaluated by t-plot, is also strongly influenced by the impregnation procedure. Indeed, while a decrease in V_{micro} is observed using impregnation route 1 and 2, a slight increase is observed when the sample is prepared using impregnation route 3 (55Ti-SBA-3-c400). Note that the last sample is also the sample presenting the highest surface area.

Isotherms shape remains almost unchanged with respect to the silica parent support (Fig. 1A, type IV isotherms). The decrease in pore volume is clearly observed on the lower N_2 volume adsorbed on the three nanocomposites, and a significant shift of the P/P_0 desorption relative pressure is also observed. While a hysteresis of type 1 is observed for the SBA support (with parallel adsorption and desorption branches), which is characteristic of cylindrical pores, the hysteresis becomes close to the type 2 for the three nanocomposites. This clearly suggests a loss in cylindrical pore shape structure. Moreover, 55Ti-SBA-1-

c400 and in a lesser extent 55Ti-SBA-2-c400 present desorptions in two steps (Fig. 1A). Applying the BJH model to the desorption branch of the isotherms gives mean pore size values varying between 3.9 nm (55Ti-SBA-1-c400) and 4.8 nm (55Ti-SBA-3-c400) (Table 1 and Fig. 1B). Due to the two-steps desorption over 55Ti-SBA-1-c400, and in a lesser extent over 55Ti-SBA-2-c400, these samples present bimodal pore size distribution, with a main porosity at 3.9 nm and a residual pore fraction at 7.5 nm, close to the initial pore size of the silica sample (Fig. 1B). Residual porosity is identified on the figure by an arrow.

3.3. Structural properties of the composites

Small-angle XRD patterns show that the hexagonal structure of the silica host support is almost maintained after the impregnation-calcination cycle whatever the impregnation procedure: the diffraction corresponding to the *(100)* crystal plane is always visible at 2θ = 9.6 nm (d_{100} value - Table 1 and Fig. 3A), showing that the pore-pore distance remains unchanged, and that titania deposition cycle does not strongly alter the silica pore structure. The *(110)* and *(200)* reflections are however visible only on the 55Ti-SBA-1-c400 sample, while broad and poorly defined diffraction signals are observed for the 55Ti-SBA-2-c400 and 55Ti-SBA-3-c400 nanocomposites. Taking into account the pore sizes measured by the BJH method for each sample, wall thickness ranging from 8.8 nm (55Ti-SBA-3-c400, Table 1) and 9.7 nm (the two other samples, Table 1) are calculated. This clearly shows some changes in titania thickness deposition, depending on the impregnation procedure. Note that the isotherms shape (evolution of the hysteresis shape, as well as the bimodal pore size distribution) suggests some partial pore plugging for 55Ti-SBA-1-c400 and 55Ti-SBA-2-c400. This pore plugging will artificially lead to smaller measured pore size, and consequently to higher wall thickness.

Important differences are also observed on the diffractograms for 2θ between 10° and 80°. While diffraction peaks assigned to the anatase structure are clearly observed for the 55Ti-SBA-1-c400 and 55Ti-SBA-2-c400 samples (Fig. 3B), the diffraction pattern obtained for the 55Ti-SBA-3-c400 sample does not exhibit such reflections suggesting that titania remains amorphous or crystallizes at a size below the detection limit of the instrument (< 4 nm). Applying the Scherrer equation to the *(101)* diffraction peak leads to average crystal sizes of 36 nm and 17 nm for 55Ti-SBA-1-c400 and 55Ti-SBA-2-c400, respectively

(Table 1). These values of mean crystal size are not compatible with a satisfying dispersion of the titania clusters inside the hexagonal porosity of the silica support. Indeed, a satisfying infiltration of the titania precursor in the porosity during impregnation would obviously lead to titania crystal sizes lower than the silica pore size. In other words, a maximum crystal size close to the pore size (further increase in crystal size would result in the destruction of the SiO_2 pore structure) is awaited. Consequently, results obtained by small angle X-ray diffraction and wide-angle X-ray diffraction suggest that a part of titania crystallizes outside the silica pore structure for the composites synthesized using impregnation procedures 1 and 2.

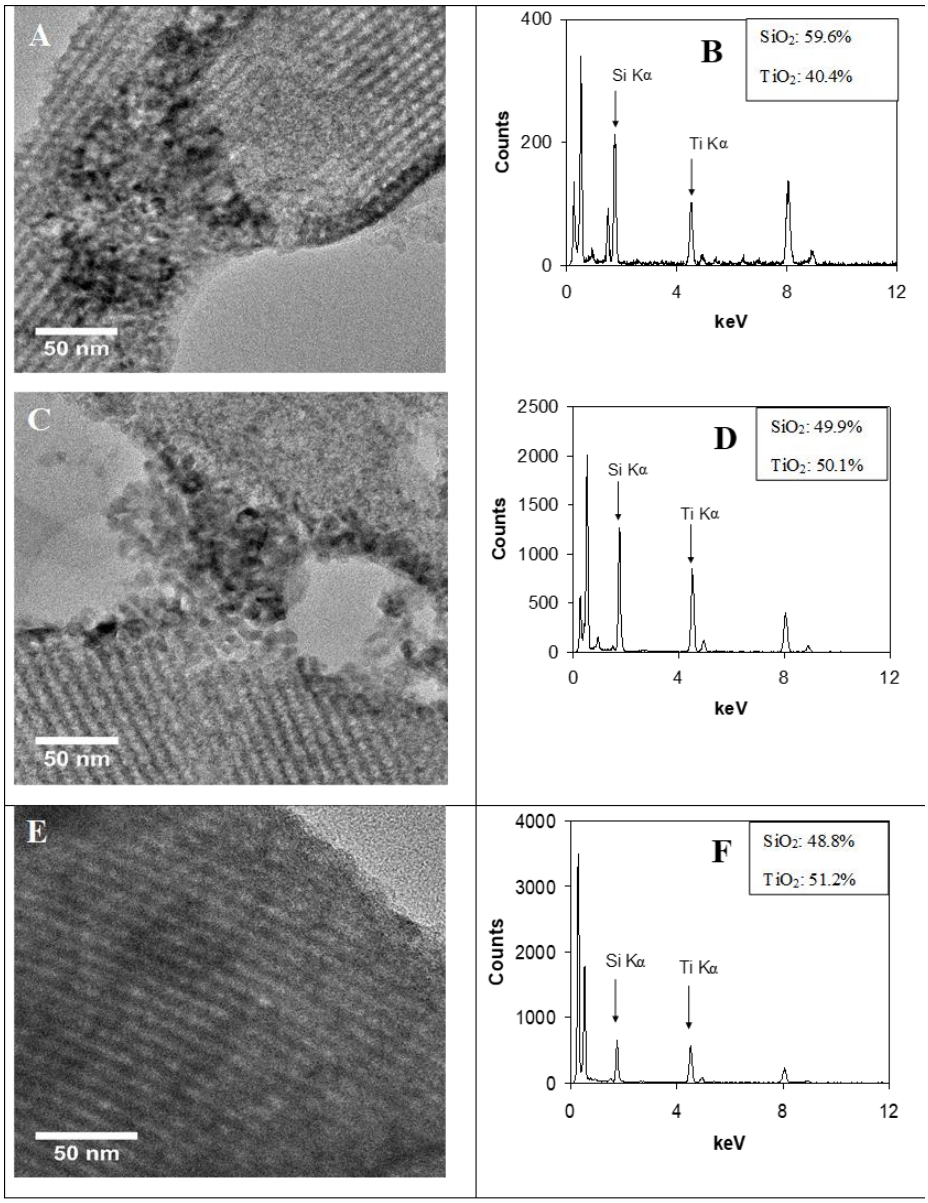

Fig. 4. Typical TEM images and representative EDX spectra obtained for the nanocomposites calcined at 400 °C. **A**, **B**: procedure 1; **C**, **D**: procedure 2; **E**, **F**: procedure 3.

TEM analysis also evidenced significant differences between the three samples. Indeed, impregnation procedure 1 leads to the formation of bulky anatase aggregates on the outer layer or outside the silica grains (Fig. 4A) showing that direct wet impregnation of $Ti(O^iPr)_4$ leads to the segregation of the precursor outside the porosity. This correlates well with the conclusions deduced from X-ray diffraction. This interpretation was further confirmed by EDX spectroscopy (Fig. 4B). Indeed, the darker aggregates are mainly composed by TiO_2, and analysis of well-defined structured zones shows largely lower TiO_2 content than the theoretical one (Fig. 4B). Better dispersion of titania is obtained using the impregnation procedure 2. Indeed, some external titania aggregates are still observed outside the silica porosity (Fig. 4C), but in a lesser extent. EDX spectroscopy shows however higher titania content inside the structured silica particles than for the 55Ti-SBA-1-c400 sample (compare Fig. 4B and D). Note that for this sample, slightly higher Ti content at the edge of the support is suggested by EDX spectroscopy. Better results are obtained using impregnation route 3 (slow infiltration of dilute $Ti(O^iPr)_4$ solution). In this last case, a careful analysis of the sample by TEM does not allow to detect external TiO_2 aggregates. The hexagonal pore structure of the sample becomes more difficult to observe than for the two other samples, but is still present (Fig. 4E). EDXS analysis gives the highest TiO_2 content among the three analyzed samples (51.2 wt.%, Fig. 4F), a value close to the theoretical content (55 wt.%).

The presence of a crystallized phase, detected by X-ray diffraction, in the case of the samples prepared using procedures 1 and 2 can be easily correlated to the morphology observed by TEM analysis. Indeed, bulky TiO_2 particles located outside the silica porosity are suggested to be responsible for the X-ray diffraction signals observed Figure 4. For the 55Ti-SBA-3-c400 sample, no external TiO_2 aggregates can be observed. Due to the open hexagonal porosity maintained by the composite (D_p decreases from 8.4 nm to 4.8 nm, Table 1), titania mean particle size is calculated at a maximum of 3.8 nm. This limited size can explain why no clear diffraction peaks can be observed for this sample. Note that the formation of an amorphous titania phase can also be a reason for the absence of diffraction peak for this sample. Then, only impregnation procedure 3 (impregnation of a dilute solution of $Ti(O^iPr)_4$) leads to a satisfying dispersion of

titania inside the silica porosity. This conclusion is supported by the characteristics of this nanocomposite which are:

No detectable crystallized phase by X-ray diffraction

No segregation of titania outside silica by TEM (and EDXS)

A specific surface area close to that of the parent support, and limited mesopore volume and pore diameter reductions

3.4. Surface properties of the composites

Oxide surfaces are generally covered by hydroxyl groups at various concentration, that greatly depends on the nature of the solid and the thermal treatment performed before analysis. An examination of the surface hydroxyl structure could provide useful information on the nature of the interaction between active phase and the oxide surface. In these lines, infrared spectroscopy is well known to be the most useful method to characterize the surface properties of the solids. Thus, IR spectra of surface hydroxyl group obtained for the modified silica samples are presented in Fig. 5A. The FT-IR spectrum of the SBA-15 reference sample (dotted line, Fig. 5A) displays a sharp band at 3745 cm^{-1} assigned to isolated SiOH groups, as reported in numerous studies [44-46]. Intensity of this band is observed to decrease with the incorporation of titania, and a new component appears at about 3720 cm^{-1}. As already reported by Bonelli et al. [47], this band can be assigned to TiOH species. Its intensity is strongly affected by the impregnation route, and a new broad band also grows simultaneously, located at 3670 cm^{-1}. This latter band has already been observed by Widenmeyer et al. [31], and is assigned to more acidic OH group observed by the authors over bulk titania materials. Comparison of the different composites (Fig. 5A) clearly shows that the titania hydroxide concentration is increasing over the nanocomposites as follows: 55Ti-SBA-1-c400 < 55Ti-SBA-2-c400 < 55Ti-SBA-3-c400. Note that the SiOH concentration is varying in the opposite way but in a less extent. The observed increase in TiOH intensity bands at 3720 cm^{-1} and 3670 cm^{-1} from procedure 1 to procedure 3 is in accordance with the previous results obtained by physical characterization. Indeed, the 55Ti-SBA-1-c400 sample presents the larger mean crystal size (d_{XRD} = 36.5 nm, Table 1) and then the lower titania accessible surface per mass unit. Logically, this sample presents the lower TiOH concentration (Fig. 5A). Conversely,

the highest dispersion (or lower TiO_2 size) is suggested for the 55Ti-SBA-3-c400 sample. This sample should present the highest titania accessible surface per mass unit which is in accordance with the highest TiOH surface concentration as clearly observed Fig. 5A.

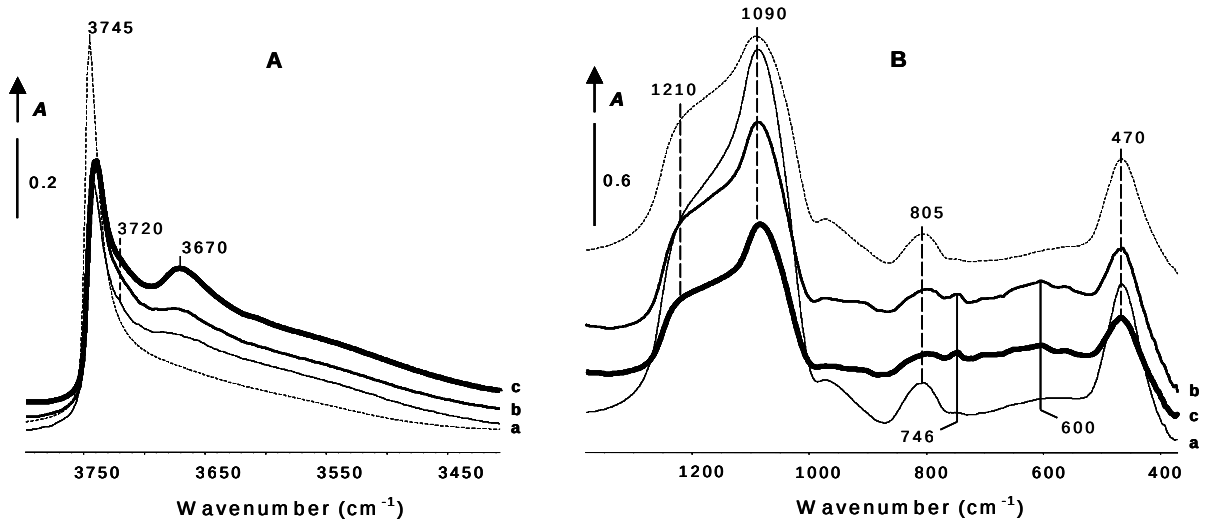

Fig. 5. IR spectra of the nanocomposites calcined at 400 °C. (A) ν(OH) region of self-supported samples after activation at 673 K and (B) KBr pellets. (a) 55Ti-SBA-1-c400; (b) 55Ti-SBA-2-c400; (c) 55Ti-SBA-3-c400; Dotted line: SBA.

The FTIR spectra skeleton (Fig. 5B) is dominated by the asymmetric and symmetric Si-O-Si stretching vibration located respectively at 1090 cm^{-1}, with shoulders at 1210 cm^{-1} and 805 cm^{-1} [48]. The band at 470 cm^{-1} is assigned to the Si-O-Si bending mode, while the band at 746 cm^{-1} is assigned to the out of plane aromatic C-H vibrations [49] probably originating from organic residual compounds from the synthesis. Spectra obtained for the samples modified by Ti incorporation are very close to that of the silica reference with only a weak addition of a component at about 600 cm^{-1}. This band is assigned to Ti-O-Ti stretching vibration. This band is especially observed on samples b and c (respectively prepared by impregnation procedures 2 and 3), which are otherwise the materials that present the higher amount of TiOH groups (Fig. 5A). Note that the presence of framework titania and vibrations of Ti-O-Si bonds can also be characterized by IR bands in the 910-960 cm^{-1} range [50]. However, the interaction between the titania phase and the silica surface remains difficult to analyze due to the presence of Si-O-Si vibration mode in this spectral region.

3.5. Thermal stability of the nanocomposites

Results of physical and structural characterizations of the three nanocomposites clearly show that the use of the impregnation procedure 3 allows to maintain a mesopore structure, originating from the silica support, and leads to an excellent dispersion of titania in the silica pores. As mentioned in the introduction part, the thermal stability of TiO_2 is one important constraint to its use as catalyst support, whatever the synthesis procedure used (precipitation or sol gel). Consequently, the thermal stability of the 55Ti-SBA-3 sample was evaluated up to 800 °C.

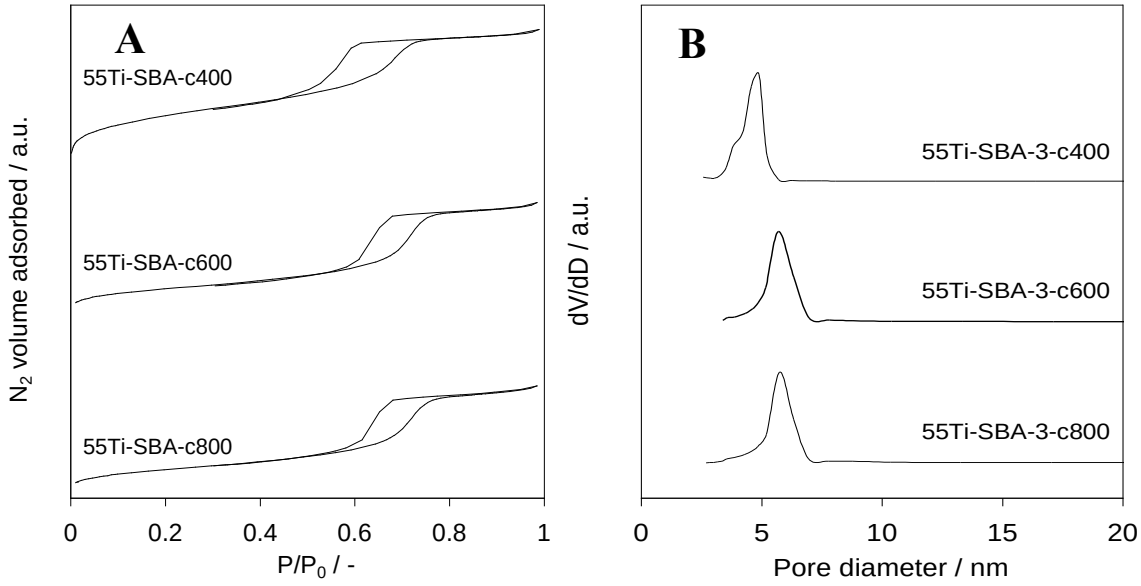

Fig. 6. N_2 adsorption – desorption isotherms and corresponding BJH pore size distribution of 55Ti-SBA-3 calcined at different temperatures.

Table 2. Effect of the calcination temperature on the physical properties of the nanocomposite prepared according to procedure 3.

Sample name	S_{BET}[a] ($m^2.g^{-1}$)	V_{meso}[a] ($cm^3.g^{-1}$)	V_{micro}[a] ($cm^3.g^{-1}$)	D_p[a] (nm)	d_{100}[b] (nm)	Wall thickness[c] (nm)	Crystal phase / d_{XRD}[d] (nm)
55Ti-SBA-3-c400	482	0.47	0.072	4.8	9.6	8.8	n.d.
55Ti-SBA-3-c600	228	0.36	0.008	5.7	9.0	7.0	Anatase / 8.1
55Ti-SBA-3-c800	204	0.35	0.001	5.7	9.1	7.2	Anatase / 10.3

[a, b, c, d]; see footnote Table 1.

N_2 adsorption-desorption isotherms obtained for the 55Ti-SBA-3 sample after calcination ranging from 400 °C and 800 °C are presented in Fig. 6A. The shape of the isotherms remains almost unchanged (type IV according to the IUPAC classification) but small changes in the hysteresis shape and on the P/P_0 adsorption and desorption relative pressures are observed. As reported in Table 2, a decrease of about 58 % of the SSA is observed increasing the calcination temperature from 400 °C to 800 °C. At the same time, a 25% decrease in mesopore volume is observed, and microporosity completely disappeared (Table 2). The BJH mean pore size is found to slightly increase, but remains upon that of the initial support whatever the calcination temperature. Then, the increase in calcination temperature leads to important modifications of the pore nanocomposite properties.

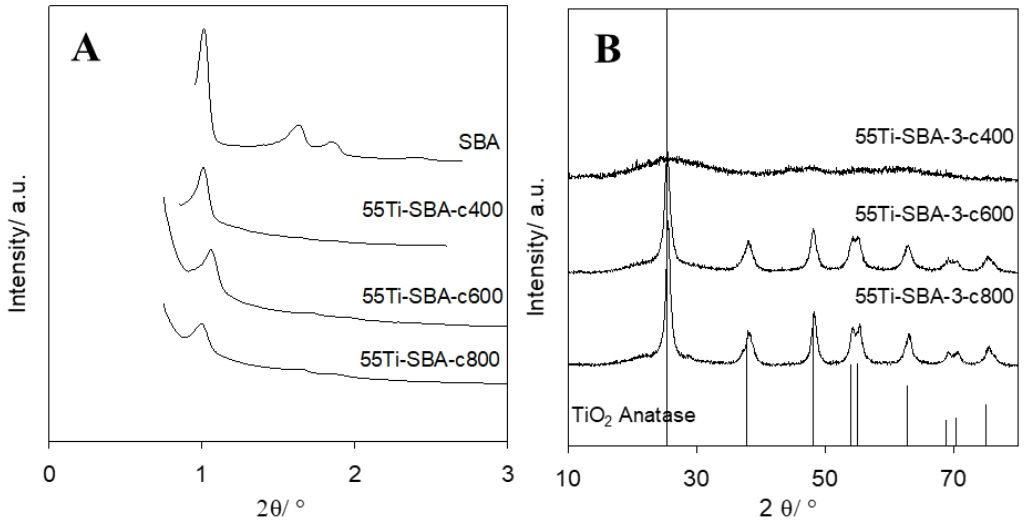

Fig . 7. Small-angle and wide-angle X-ray diffraction patterns of 55Ti-SBA-3 calcined at different temperatures.

Small angle X-ray diffraction (Fig. 7A) and TEM micrographs (not showed) suggest that these changes in physical properties are not originating from an important alteration of the silica pore structure. Indeed, small-angle X-ray diffraction always evidenced the presence of the *(100)* diffraction of the hexagonal structure (Fig. 7A), whatever the calcination temperature. From the *(100)* diffraction peak position, and taken into account the BJH pore size, the wall thickness is found to slightly decrease when the temperature of calcination increases (Table 2). Moreover, the increase in calcination temperature seems to result in an easier detection of the *(200)* and *(110)* diffraction peaks. TEM micrographs also evidence the maintain of the

hexagonal pore structure, even after calcination at 800 °C (not showed). Focus on the pore allows to detect crystallized nanoparticles (Fig. 8A-C).

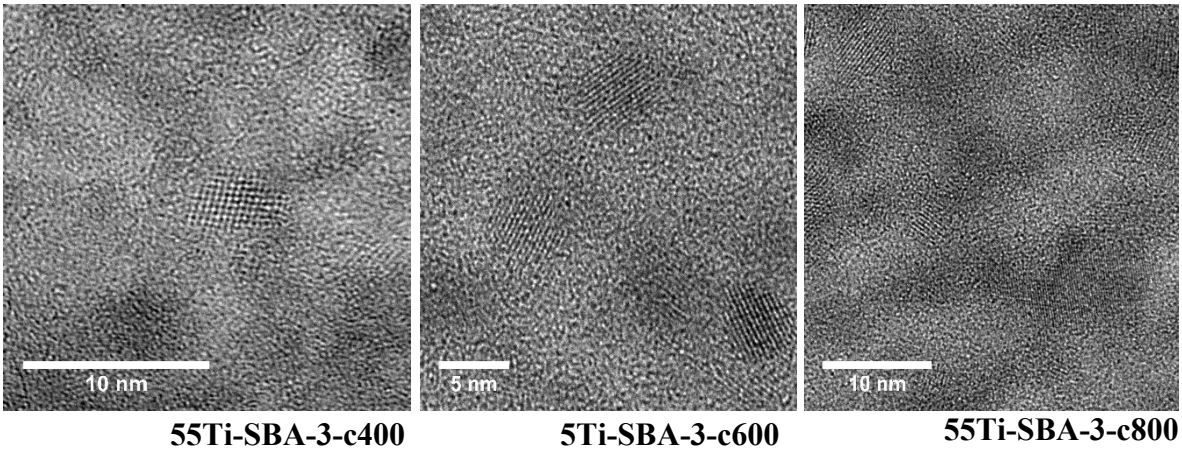

Fig. 8. TEM images of 55Ti-SBA-3 calcined at different temperatures.

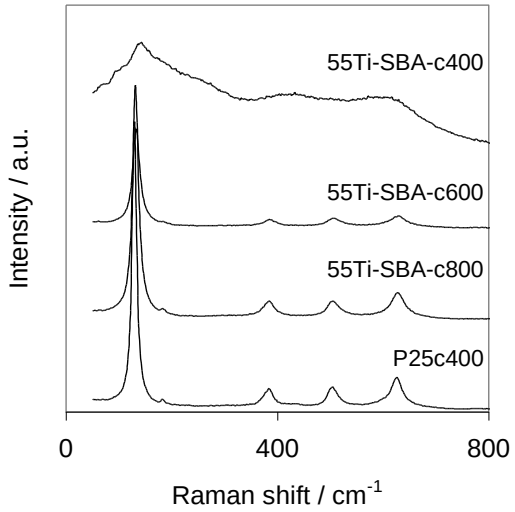

Fig. 9. Raman spectra of 55Ti-SBA-3 calcined at different temperatures. Comparison with a reference P25 sample from Degussa.

It is interesting to note that even if the sample is calcined at only 400 °C and no diffraction peaks attributed to the anatase structure can be observed (Fig. 7B), crystallized nanoparticles (< 4 nm) are observed by TEM. This suggests that the small size of the anatase nanoparticles is responsible for the lack in X-ray reflections. At higher calcination temperatures (600-800 °C), anatase patterns are clearly identified (Fig. 7B). The evaluation of the mean particle size from the broadening of the X-ray diffraction lines leads to particle sizes of 8.1 nm and 10.3 nm for 55Ti-SBA-3-c600 and 55Ti-SBA-3-c800, respectively (Table 2). Note that d_{XRD} seems larger than those observed on the TEM micrographs (Fig. 8), but are in the range of the BJH pore size measured for the silica support alone (8.4 nm, Table 1). As concluded from TEM and X-ray

diffraction measurements, further analysis by Raman spectroscopy (Fig. 9) confirms the presence of a well-crystallized anatase phase after calcination at 600 °C and 800 °C, with experimental spectra close to that of the reference P25 spectrum. The three spectra exhibit five characteristic bands, located at 140 cm^{-1} (E_g), 200 cm^{-1} (E_g), 390 cm^{-1} (B_{1g}), 512 cm^{-1} (B_{2g}) and 639 cm^{-1} (E_g). These spectra are similar to those reported in Raman studies for pure anatase phases [51-54]. A broad shoulder at 447 cm^{-1} (E_g), characteristic of the rutile phase, is also observed on the P25 spectrum. For the 55Ti-SBA-3-c400, broad and weak reflections of the anatase structure are observed. The poor definition of the Raman spectrum obtained after calcination at 400 °C can obviously be related to the low titania crystal size in this nanocomposite, leading to the widening of the signal and decrease in Raman signal intensity. This confirms, as suggested by TEM, that the titania phase is in the form of anatase nanodomains (avoiding its detection by X-ray diffraction) when nanocomposite is calcined at only 400 °C.

Consequently, the increase in calcination temperature leads to a progressive sintering of the titania nanoparticles from a few nanometers to large 8-10 nm particles. These particles are clearly identified by TEM, and remain located inside the silica pores after sintering. Thus, a pore plugging phenomenon occurring when calcination temperature exceeds 600 °C can explain the change in physical properties, especially the decrease in S_{BET} and V_{meso} (Table 2). Conversely to bulk titania sample (Degussa P25), the calcination up to 800 °C of the nanocomposites does not lead to the crystallization of the rutile phase. Indeed, diffraction patterns obtained for the P25 samples (not showed) evidenced the crystallization of a pure rutile phase since 600 °C. The interaction of the titania phase with the support can be a reason of the delay in phase transition. The reduced size of the porosity of the silica support (< 10 nm), that leads to a maximum titania crystal size by confining effect, can also explain the absence of anatase to rutile transition even at 800 °C. Indeed, while titania exists in different polymorphs, thermodynamic stability of the three polymorphs (anatase, brookite and rutile) is reported to be size dependant. Rutile macrocrystals are then reported to be thermodynamically more stable than the two other polymorphs while the nanocrystalline (< 14 nm) anatase and brookite polymorphs are more stable than rutile [3, 55]

Discussion

Increasing both specific surface area and thermal stability of titania is a real challenge. As an example, the use of a mixed-oxide SiO_2 – TiO_2 is reported to be interesting because of the non – photoactivity of SiO_2, and the higher activity developed by the mixed-oxide [56]. Among the samples prepared, only the 55Ti-SBA-3-c400 sample is found to present an homogeneous dispersion of the titania in the pore structure of the host support. Indeed, a high surface area, close to that of the initial host support, is obtained over this sample while a decrease in surface area is observed using the two other impregnation procedures (55Ti-SBA-1-c400 and 55Ti-SBA-2-c400, Table 1). It is clear from the results that the quantity of ethanol used for the impregnation step is of great importance to obtain a homogeneous nanocomposite, *i.e.* without segregation of the titania precursor outside the silica porosity. As proposed by Cassiers et al. [56], ethanol can facilitate the grafting of $Ti(O^iPr)_4$ precursor onto the Si-OH groups. As observed by the authors, the nature of alcohol used is not crucial, and other alcohol can be used [57].

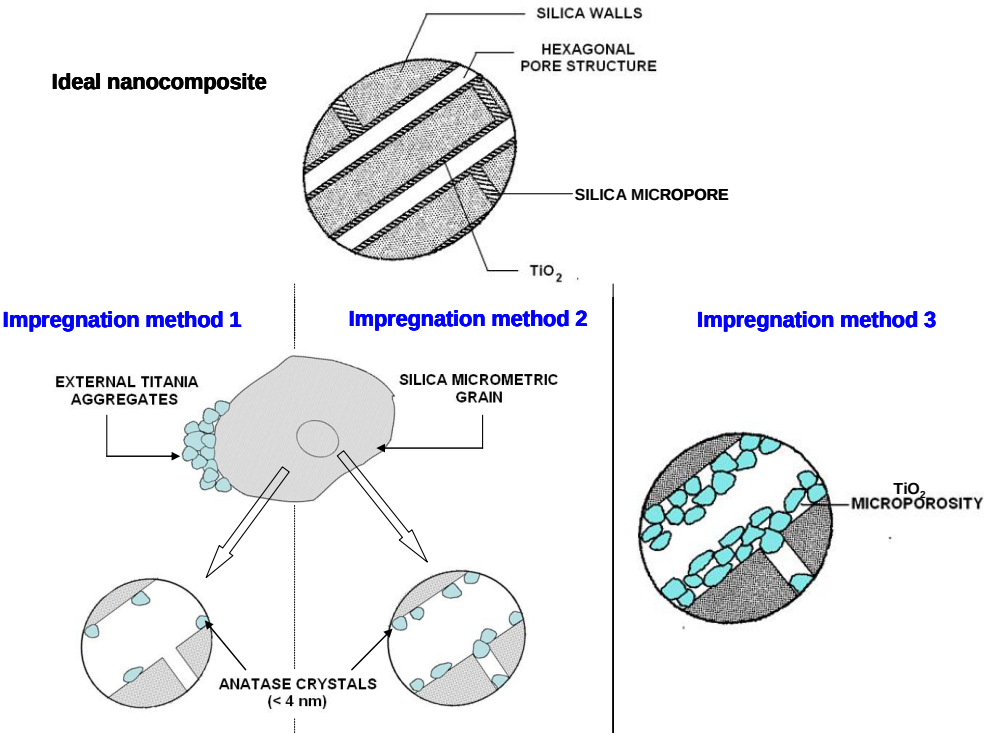

Scheme 1. Representation of the morphology of the three TiO_2-SiO_2 composites.

An ideal composite can be described by a titania film formed at the surface of the cylindrical pores of the silica (Scheme 1). Nevertheless, it is difficult to obtain a fine crystalline film (1-2 nm), and crystallization of titania results in the formation of nanodomains of few nanometers (Fig. 8). Among the prepared composites, the sample synthesized without ethanol (55Ti-SBA-1-c400), as well as the sample prepared with a low quantity of ethanol (55Ti-SBA-2-c400) exhibits some large anatase segregation outside the silica porosity (see Fig. 4). Consequently, the loading of the silica porosity is lower than the theoretical one. This is schematized Scheme 1, by a low titania nanodomain content in the pore, and the formation of external titania aggregates. Conversely, the composite synthesized using a dilute solution of titania precursor (55Ti-SBA-3-c400) does not present such titania segregation. Moreover, no diffraction peak assigned to the anatase structure can be observed by X-ray diffraction, and this composite presents the highest TiOH density. Complementary characterizations by TEM and Raman spectroscopy clearly suggest that the lack in anatase reflexion is not attributed to the formation of an amorphous titania phase but is originating from the limited size of the nanocrystals formed inside the porosity. Indeed, TEM evidenced the formation of < 4 nm crystals while Raman spectroscopy evidenced a typical signal of the anatase structure. In addition, this sample presents the lowest decrease in pore size and mesopore volume, with D_p = 4.8 nm and V_{meso} = 0.47 $cm^3.g^{-1}$ (Table 1). Assuming an anatase density of 3.72 $g.cm^{-3}$ and the formation of a non porous film covering uniformly the surface of the silica pore, a theoretical pore size of 4.5 nm and a mesopore volume of 0.43 $cm^3.g^{-1}$ are obtained. The theoretical values of pore size and mesopore volume are close to the experimental ones, supporting the interpretation of a homogeneous dispersion of the titania in the pore and a limited pore plugging. In addition, the specific surface area of the nanocomposite is maintained at 482 $m^2.g^{-1}$, showing that the titania phase developed a surface area close to 470 $m^2.g^{-1}$, the surface area of the initial support (Table 1). Similar SSA for the support and for the TiO_2 phase is purely coincidental, and the use of a support having higher SSA would obviously lead to a decrease of the nanocomposite SSA. The calculated crystal domain size to develop this surface, assuming cubic particles, is 3.2 nm. This theoretical crystal size is also close to that directly observed by TEM, evidenced to be lower than 4 nm. Then, the morphology of the 55Ti-SBA-3-c400 nanocomposite can be represented as a stacking of small titania nanodomains in the

silica pores (Scheme 1). This stacking can also explain why a maintain of the microporosity is observed for this sample, and not for the two other composites (Table 1).

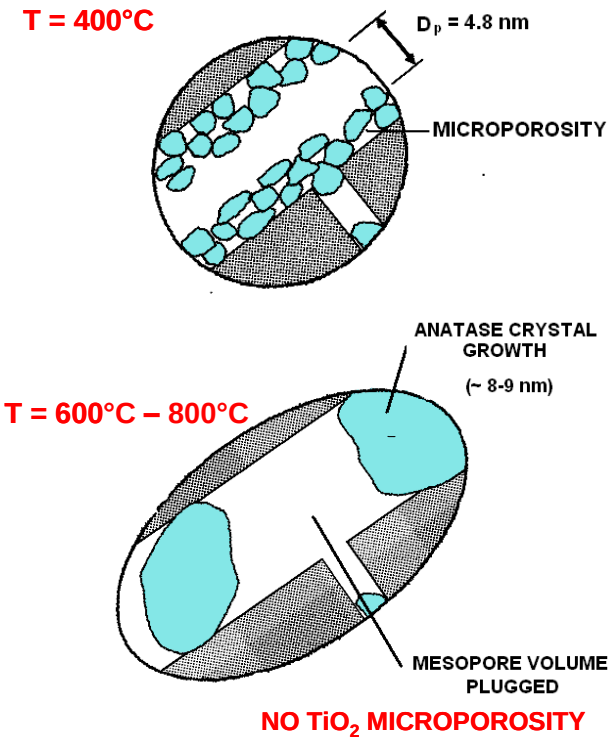

Scheme 2. Evolution of the nanocomposite morphology with the calcination temperature. Example of the 55Ti-SBA-3 sample.

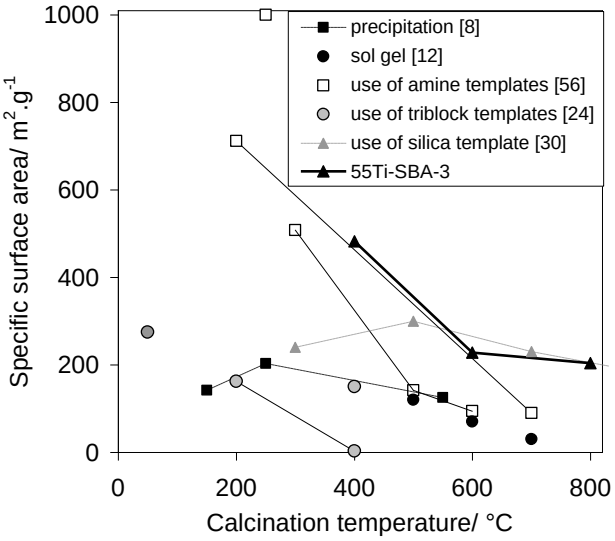

Figure 10. Comparison of the SSA obtained on the 55Ti-SBA-3 sample calcined at different temperatures with some significant academic references.

When calcination temperature increases, the titania nanodomains agglomerate to form ~10 nm TiO_2 anatase crystals. This crystal shrinkage results in some pore plugging, leading to an important decrease in surface area and mesopore volume. It is interesting to note that even after calcination at 800 °C, no anatase to rutile transition and no important crystal growth can be observed. Indeed, the crystal domain size obtained after calcination at 800 °C is 10.3 nm (Table 2), a value close to the silica pore size (8.4 nm, Table 1). This clearly suggests a limitation of the crystal growth by the silica host support. This mechanism is presented Scheme 2. Using a similar approach, Lee et al. [29, 30] obtained TiO_2 samples having SSA that can reach 300 $m^2.g^{-1}$ at 500 °C but a decrease up to 180 $m^2.g^{-1}$ is observed with the increase in calcination temperature at 900 °C (the sample is prepared by nanocasting using a silica template) (Fig. 10). Examples of thermal stability dealing with bulk titania solids are numerous (see Fig. 10), but important decreases in SSA are always reported. Focus on the 400 °C – 800 °C zone of Fig. 10 shows that the 55Ti-SBA-3 nanocomposite presents SSA quite higher than the other solids. Nevertheless, a part of the surface developed by the nanocomposite is originating from the silica support. The limited size of the titania crystal (~ 10 nm) however suggests that nanocluster growth can be physically limited, leading to titania particles presenting significant surface area, even after high temperature treatment.

Conclusion

This work reports the synthesis of mesostructured TiO_2/SiO_2 nanocomposite. Synthesis procedure is based on the impregnation of titanium alkoxide in a short-chain alcohol. Under specific conditions, it is possible to obtain a nanocomposite of "high quality", *i.e.* having a homogeneous dispersion of titania nanodomains in the porosity of the silica host support. When a homogeneous dispersion of the titania phase is obtained, the nanocomposite presents excellent physical properties if calcined at low temperature (400 °C). Indeed, a specific surface area close to that of the silica support is obtained (482 $m^2.g^{-1}$) and no alteration of the silica pore structure can be evidenced. While no crystallized phase are observed by X-ray diffraction, TEM and Raman spectroscopy suggest the presence of anatase nanodomains (~ 2-3 nm).

Increasing the calcination temperature up to 800 °C leads to the sintering of the titania nanodomains up to a size close to that of the silica pore size. This clearly suggests a limitation of the crystal growth by the inorganic walls of the support. As a consequence, sintering of the titania crystal domains leads to a significant mesopore plugging, and decreases of the composite pore volume and surface area. The resulting composites still present quite high SSA after calcination at high temperature (> 204 $m^2.g^{-1}$) and limited anatase crystal size (< 10.3 nm).

ACKNOWLEDGMENT

The *Région Poitou-Charentes*, France, is acknowledged for the financial support of this work through a Ph.D. grant (M. Bonne). Mme Danielle Mesnard is acknowledged for Raman experiments.

REFERENCES

[1] Reyes-Coronado D., Rodriguez-Gattorno G., Espinosa-Pesqueira M., Gardner J.M., Meyer G.J., Oskam G., Proceeding of SPIE (2007) 6650.

[2] Koelsch M., Cassaignon S., Guillemoles J.F., Jolivet J.P., Thin Solid Films 403-404 (2002) 312.

[3] Zhang H., Banfield J.F., J. Mater. Chem. 8 (1998) 2073.

[4] Ambrus Z., Mogyorósi K., Szalai Á., Alapi T., Demeter K., Dombi A., Sipos P., Appl. Catal. A : General 340 (2008) 153.

[5] Ye X., Chen. D., Li K., Shah V., Kesmez M., Vajifdar K., Chem. Eng. Commun. 194 (2007) 368.

[6] Vlachos P., Stathatos E., Lyberatos G., Lianos P., Catal. Commun. 9 (2008) 1987.

[7] Grosso D., Soler-Illia G.J. de A.A., Crepaldi E.L., Cagnol F., Sinturel C., Bourgeois A., Brunet-Bruneau A., Amenitsch H., Albouy P.A., Sanchez C., Chem. Mater. 15 (2003) 4562.

[8] Elshafei G.M.S., Philip C.A., Moussa N.A., Micro. Meso. Mater. 79 (2005) 253.

[9] Iwasaki M., Hara M., Ito S., J. Mat. Sc. Lett. 17 (1998) 1769.

[10] Aguado-Serrano J., Rojas-Cervantes M.L., Micro. Meso. Mater. 88 (2006) 205.

[11] Liu C., Fu L., Economy J., J. Mater. Chem. 14 (2004) 1187.

[12] Sreethawong T., Suzuki Y., Yoshikawa S., Catal. Commun. 6 (2005) 119.

[13] Antonelli D.M., Micro. Meso. Mater. 30 (1999) 315.

[14] Yoshitake H., Sugihara T., Tatsumi T., Chem. Mater. 14 (2002) 1023.

[15] Yoshitake H., Tatsumi T., Chem. Mater. 15 (2003) 1695.

[16] Yang P., Zhao D., Margolese D.I., Chmelka B.F., Stucky G.D., Chem. Mater. 11 (1999) 2813.

[17] Alberius P.C.A., Frindell K.L., Hayward R.C., Edward J.K., Stucky G.D., Chmelka B.F., Chem. Mater. 14 (2002) 3284.

[18] Luo H., Wang C., Yan Y., Chem. Mater. 15 (2003) 3841.

[19] Smarsly B., Grosso D., Brezesinski T., Pinna N., Boissière C., Antonietti M., Sanchez C., Chem. Mater. 16 (2004) 2948.

[20] Haseloh S., Choi S.Y., Mamak M., Coombs N., Petrov S., Chopra N., Ozin G.A., Chem. Commun. (2004) 1460.

[21] Kartini I., Meredith P., Diniz Da Costa J.C., Lu G.Q., J. Sol-gel. Sc. Technol. 31 (2004) 185.

[22] Kartini I., Menzies D., Blake D., Da Costa J.C.D., Meredith P., Riches J.D., Lu G.Q., J. Mater. Chem. 14 (2004) 2917.

[23] Eiden-Assmann S., Widoniak J., Maret G., Chem. Mater. 16 (2004) 6.

[24] Widoniak J., Eiden-Assmann S., Maret G., Prog. Colloid Polym. Sci. 129 (2004) 119.

[25] Wu C.-W., Ohsuna T., Kuwabara M., Kuroda K., J. Am. Chem. Soc. 128 (2006) 4544.

[26] Khushalani D., Ozin G.A., Kuperman A., J. Mater. Chem. 9 (1999) 1491.

[27] Soller-Illia G.J. de A.A., Louis A., Sanchez C., Chem. Mater. 14 (2002) 750.

[28] Shibata H., Ogura T., Mukai T., Ohkubo T., Sakai H., Abe M., J. Am. Chem. Soc. 127 (2005) 16396.

[29] Lee D.-W., Ihm S.-K., Lee K.-H., Chem. Mater. 17 (2005) 4461.

[30] Lee D.-W., Park S.-J., Ihm S.-K., Lee K.-H., Chem. Mater. 19 (2007) 937.

[31] Widenmeyer M., Grasser S., Köhler K., Anwander R., Micro. Meso. Mater. 44-45 (2001) 327.

[32] Cozzolino M., Di Serio M., Tesser R., Santacesaria E., Appl. Catal. A: General 325 (2007) 256.

[33] Lin Y.C., Chang C. H., Chen C .C., Jehng J.-M., Shyu S.-G., Catal. Comm. 9 (2008) 675.

[34] Vinu A., Srinivasu P., Sawant D.P., Alam S., Mori T., Ariga K., Balasubramanian V.V., Anand C., Micro. Meso. Mater. 110 (2008) 422.

[35] Zhang W.H., Lu J., Han B., Li M., Xiu J., Ying P., Li C., Chem. Mater. 14 (2002) 3413.

[36] Dong W., Sun Y., Wee Lee C., Hua W., Lu X., Shi Y., Zhang S., Chen J., Zhao D., J. Am. Chem. Soc. 129 (2007) 13894.

[37] Bérubé F., Kleitz F., Kaliaguine S., J. Mater. Sci., in press.

[38] Fattakhova-Rohlfing D., Szeifert J.M., Yu Q., Kalousek V., Rathouskỳ J., Bein T., Chem. Mater. 21 (2009) 2410.

[39] Bonne M., Bion N., Pailloux F., Valange S., Royer S., Tatibouët J.-M., Duprez D., Chem. Commun. (2008) 4504.

[40] Roggenbuck J., Koch G., Tiemann M., Chem. Mater. 18 (2006) 4151.

[41] Sing K.S.W., Everett D.H., Haul R.H.W., Moscou L., Pierotti R.A., Rouquerol J., Siemieniewska T., Appl. Chem. 57 (1985) 603.

[42] Kruk M., Jaroniec M., Ko C. H., Ryoo R., Chem. Mater. 12 (2000) 1961.

[43] Ryoo R., Ko C. H., Kurk M., Antochshuk V., Jaroniec M., J. Phys. Chem. B 104 (2000) 11465.

[44] Manoilova O.V., Dakka J., Sheldon R.A., Tsyganenko A.A., Stud. Surf. Sci. Catal. 94 (1995) 63.

[45] Knözinger H., Huber S., J. Chem. Soc. Faraday Trans. 94 (1998) 2047.

[46] Trukhan N.N., Panchenko A.A, Roduner E., Langmuir 21 (2005) 10545.

[47] Bonelli B., Cozzolino M., Tesser R., Di Serio M., Piumetti M., Garrone E., Santacesaria E. J., Catal. 246 (2007) 293.

[48] Zeleňák V., Hornebecq V., Mornet S., Schäf O., Llewellyn P., Chem. Mater. 18 (2006) 3184.

[49] Coutinho D., Acevedo A.O., Dieckmann G.R., Balkus K.J., Micro. Meso. Mater. 54 (2002) 249.

[50] Armaroli T., Milella F., Notari B., Willey R.J., Busca G., Topics in catalysis 15 (2001) 63.

[51] Busca G., Ramis G., Amores J.M.G., Piaggio V.S., J. Chem. Soc. Faraday Trans. 90 (1994) 3181.

[52] Mao Y., Wong S.S., J. Am. Chem. Soc. 128 (2006) 8217.

[53] Pighini C., Thèse de Doctorat, Université de Bourgogne (2006).

[54] Ivanda M., Musić S., Gotić M., Turković A., Tonejc A.M., Gamulin O., J. Mol. Struct. 480 (1999) 641.

[55] Zhang H., Banfield J. F., J. Phys. Chem. B 104 (2000) 3481.

[56] Cassiers K., Linssen T. Mathieu M., Bai Y.Q., Zhu H.Y., Cool P., Vansant E.F., J. Phys. Chem. B 108 (2004) 3713.

[57] Wang W., Song M., Mater. Res. Bull. 41 (2006) 436.